

Boundary-aware Contrastive Learning for Semi-supervised Nuclei Instance Segmentation

Ye Zhang¹

ZHANGYE94@STU.HIT.EDU.CN

Ziyue Wang¹

200111326@STU.HIT.EDU.CN

Yifeng Wang²

WANGYIFENG@STU.HIT.EDU.CN

Hao Bian³

H2495067728@GMAIL.COM

Linghan Cai¹

CEILINGHANS@GMAIL.COM

Hengrui Li⁴

23B903028@STU.HIT.EDU.CN

Lingbo Zhang³

ZHANG-LB23@MAILS.TSINGHUA.EDU.CN

Yongbing Zhang¹

YBZHANG@HIT.EDU.CN

¹ School of Computer Science and Technology, Harbin Institute of Technology, 518055, China.

² School of Science, Harbin Institute of Technology, 518055, China.

³ Tsinghua Shenzhen International Graduate School, Tsinghua University, 518071, China.

⁴ Faculty of Computing, Harbin Institute of Technology, 150001, China.

Editors: Under Review for MIDL 2024

Abstract

Semi-supervised segmentation methods have demonstrated promising results in natural scenarios, providing a solution to reduce dependency on manual annotation. However, these methods face significant challenges when directly applied to pathological images due to the subtle color differences between nuclei and tissues, as well as the significant morphological variations among nuclei. Consequently, the generated pseudo-labels often contain much noise, especially at the nuclei boundaries. To address the above problem, this paper proposes a boundary-aware contrastive learning network to denoise the boundary noise in a semi-supervised nuclei segmentation task. The model has two key designs: a low-resolution denoising (LRD) module and a cross-RoI contrastive learning (CRC) module. The LRD improves the smoothness of the nuclei boundary by pseudo-labels denoising, and the CRC enhances the discrimination between foreground and background by boundary feature contrastive learning. We conduct extensive experiments to demonstrate the superiority of our proposed method over existing semi-supervised instance segmentation methods.

Keywords: Semi-supervised learning, Nuclei instance segmentation, Edge denoising, Contrastive learning.

1. Introduction

Nuclei instance segmentation is essential in the quantitative analysis of pathological images. The characteristics of nuclei, including their size, morphology, and distribution, can provide valuable insights into the tumor immune microenvironment, thereby offering crucial support for cancer diagnosis, staging, and grading processes (Khened et al., 2021; Hollandi et al., 2022). In recent years, deep learning techniques have made remarkable advancements in nuclei segmentation. DCAN (Chen et al., 2016) adopts a dual-branch decoder architecture to predict semantics and contours simultaneously to enhance the instance distinguishing.

HoverNet (Graham et al., 2019) incorporates distance and gradient constraints to split individual instances effectively. Similar methods such as Dist (Naylor et al., 2018), CDNet (He et al., 2021), and CellPose (Stringer et al., 2021) are also proposed to address overlapping nuclei challenges. However, these supervised methods typically rely on pixel-level annotations, which are time-consuming and labor-intensive and need professional guidance, hindering the development of models. Therefore, developing a technique that can effectively address the dependency on manual annotation for nuclei instance segmentation is crucial.

A common approach to address the problem of scarce labeled data is semi-supervised learning (Reddy et al., 2018; Van Engelen and Hoos, 2020). During the training process, abundant unlabeled and insufficient labeled data are used to train the network. The existing semi-supervised methods mainly leverage prior information to improve the pseudo-label quality. For example, ShapeProp (Zhou et al., 2020b) combines the information from bounding boxes and partially annotated masks to improve the segmentation accuracy of target regions based on Mask R-CNN (He et al., 2017). PAIS (Hu et al., 2023) uses a dynamic alignment loss to address the misalignment problem between classification and segmentation results, and then a new threshold filtering method for pseudo-labels is proposed. PointWSIS (Kim et al., 2023) balances false negative and false positive errors by utilizing point supervision prior information. However, due to the low color contrast differences between the nuclei and tissues, these methods still have defects in generating nuclear pseudo-labels, limiting the application of semi-supervised instance segmentation in pathological images.

Some methods use pseudo-label optimization strategies to enhance nuclei segmentation accuracy in semi-supervised scenarios. MMT-PSM (Zhou et al., 2020a) integrates multiple data-augmented segmentation results to construct reliable predictions and enhance pseudo-labels’ confidence. CDCL (Wu et al., 2022) uses feature contrastive learning to promote feature consistency between the teacher and student networks, thus improving the quality of pseudo-labels. PG-FANet (Jin et al., 2024) employs a pseudo-label guided module that aggregates multi-scale, multi-stage features to enhance segmentation performance. However, nuclei exhibit diversity in morphology and size, and in cases with limited annotations, it is challenging for the teacher network to capture the complete range of nuclei shape features. Consequently, the generated pseudo-labels often contain edge noise because existing pseudo-label optimization methods lack specific designs for denoising nuclei boundaries, which always leads to inaccurate nuclei boundary predictions.

In this paper, to address the issue of boundary noise in nuclei segmentation, we propose a coarse-to-fine **boundary-aware** contrastive learning network for semi-supervised nuclei segmentation (BASS¹). Firstly, we design a low-resolution denoising (LRD) segmentation head that promotes boundary smoothness. Additionally, within this segmentation head, we use a low-weight loss for the nuclei boundary region optimization, which reduces the impact of uncertain boundary prediction during training. Secondly, to minimize boundary noise further, we design a cross-RoI contrastive learning (CRC) module that finely partitions the internal, external, and boundary regions of nuclei, enhancing the discriminative capability of nuclei boundary features. To demonstrate the effectiveness of our proposed method, we conduct comparative experiments and ablation studies on two public datasets. The

1. Our code is available at <https://github.com/zhangye-zoe/BASS>.

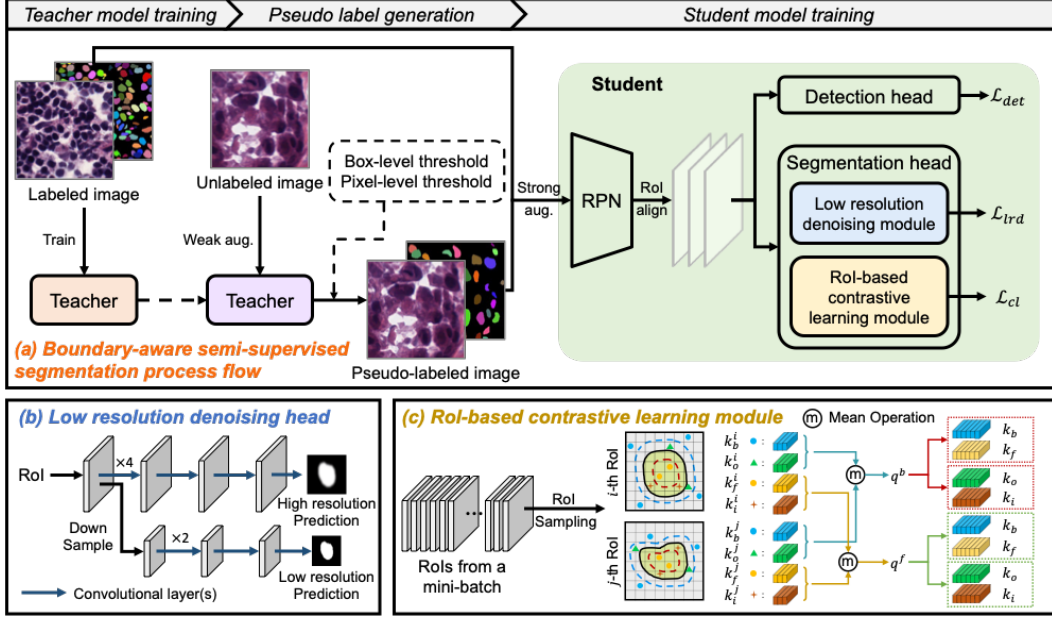


Figure 1: The framework of our semi-supervised nuclei segmentation method. (a) The training flow of our BASS. First, the teacher model generates pseudo-labels, and then the student model is used to train the nuclei segmentation network. (b) and (c) is the proposed low-resolution denoising module and cross-RoI contrastive learning module.

experimental results show that our proposed method outperforms existing semi-supervised methods, and the ablation studies demonstrate the effectiveness of the proposed modules.

2. Methodology

2.1. Framework Overview

To address the boundary noise problem of nuclei segmentation under a semi-supervised scenario, we propose a coarse-to-fine boundary-aware denoising model, as shown in Fig. 1. Our whole training process can be divided into three stages. First, the labeled data $D_L = \{(x_i, y_i)\}_{i=1}^N$ is used to train a teacher model. In this step, we employ Mask R-CNN (He et al., 2017) as the baseline, and the loss function of the teacher network is defined as follows:

$$Loss^t = L_{seg}^t + L_{det}^t, \quad (1)$$

where L_{seg}^t is the loss of the segmentation head, and L_{det}^t is the loss of the detection head, which consists of the classification loss and regression loss. Then, the trained teacher network is employed to generate pseudo-labels y_j^p for input x_j . To reduce the uncertainty of pseudo-labels, we employ box and pixel threshold filtering to generate high-confidence pseudo-labels. Finally, we combine the labeled data D_L and the generated pseudo-labeled data $D_U = \{(x_j, y_j^p)\}_{j=1}^M$ to train the student network.

In the student network, our developed denoising methods are shown in the green box of Fig. 1, which consists of a low-resolution denoising (LRD) module and a cross-RoI contrastive learning (CRC) module. The LRD employs low-resolution pseudo-labels as supervision

information to promote the smoothness of nuclei contours. Meanwhile, the CRC utilizes boundary-aware contrastive learning to enhance the discriminative capability of contour features. In the training process, the overall loss is designed as follows:

$$Loss^s = L_{det}^s + L_{nmh} + L_{lrd} + L_{cl}, \quad (2)$$

where L_{nmh} represents the naive high resolution segmentation loss, L_{lrd} represents the low-resolution segmentation loss, and L_{cl} represents the contrastive learning loss.

2.2. Threshold Filtering

Before training the student network, we choose high-confidence instances as the pseudo-labels to alleviate the influence of uncertain samples on the student network training. The teacher network outputs probability values for instances (box value) and mask probabilities (pixel value) in the inference stage. We consider the pixel-level filtering to be the hyperparameter selection. As for the box-level filtering, we choose it based on the nuclear number distribution of unlabeled data. We assume the nuclear number distribution is consistent between labeled and unlabeled data. Based on this assumption, we uniformly sample 91 values between 0.1 and 1.0. Then, we iteratively apply these probabilities to filter the instances and calculate the number distribution of nuclei in the unlabeled data. Finally, we select the threshold closest to the distribution of labeled data. We validate the effectiveness of this threshold filtering method in ablation experiments.

2.3. Low-resolution Denoising Module

In the naive Mask R-CNN (He et al., 2017), the RoI head outputs a 14×14 feature map containing boundary noise. In the subsequent convolution process, Mask R-CNN increases the feature map to capture semantic information in a larger size, but the boundary noise is also amplified. To avoid amplified noise effects, we design a low-resolution denoising module as shown in Fig.1(b), which utilizes the low-resolution pseudo-labels as supervision for model training. In the LRD, BASS directly performs segmentation in the 14×14 feature map. This approach effectively smooths the boundaries and initially reduces the noise in nuclei boundaries. Furthermore, to minimize the impact of boundary uncertainty on segmentation, we apply a weighted loss to the low-resolution segmentation head. Specifically, pixels in the boundary region are assigned a lower weight, and other areas are set to a high weight.

According to previous studies (Wang et al., 2022), although low-resolution images can reduce the boundary noise, they lose some detailed information. To preserve the details, we parallel the original segmentation head and low-resolution prediction head to perform the segmentation task simultaneously, as shown in Fig.1(b). In this manner, the output mask head decreases the influence of the original feature noise and keeps more details.

2.4. Cross-RoI Contrastive Learning

In the subsection, we propose an elaborate denoising method named cross-RoI contrastive learning. It leverages labeled data to train a boundary feature extraction module, and then the module is applied to learn the embedding of unlabeled data, which can mitigate the impact of boundary noise caused by pseudo-labels and enhance the feature discrimination

ability of foreground and background. In general, object boundaries typically correspond to hard-to-classify samples, and their embeddings are highly unstable. To avoid the impact of features from difficult samples on the representation of easy-to-classify samples, we employ region-based contrastive learning and our proposed CRC is shown in Fig.1 (c).

First, the input image x is fed into the network for feature extraction and alignment, resulting in two aligned RoI features f_i and f_j . Based on the contour (plotted in black line) shown in Fig. 1(c), we split the feature maps into foreground region \mathcal{F} and background region \mathcal{B} . By shrinking and expanding d distances, we obtain the inner contour (plotted in red dotted line) and outer contour (plotted in blue dotted line). The regions between them and the true contour are represented as the inner boundary and outer boundary. These boundary regions correspond to challenging pixels for classification and can be expressed using the following formula:

$$\begin{aligned}\mathcal{R}_i &= \{p_i | p_i \in \mathcal{F} \text{ and } \|p_i, c_i\|_2^2 \leq d\}, \\ \mathcal{R}_o &= \{p_i | p_i \in \mathcal{B} \text{ and } \|p_i, c_i\|_2^2 \leq d\}.\end{aligned}\tag{3}$$

where c_i represents the contour pixel closest to pixel p_i . At the same time, we also sample the foreground and background pixels, which can be expressed as the following equations:

$$\begin{aligned}\mathcal{R}_f &= \{p_i | p_i \in \mathcal{F} \text{ and } p_i \notin \mathcal{R}_i\}, \\ \mathcal{R}_b &= \{p_i | p_i \in \mathcal{B} \text{ and } p_i \notin \mathcal{R}_o\},\end{aligned}\tag{4}$$

where \mathcal{R}_f represents the set of pixels obtained by excluding \mathcal{R}_i from \mathcal{F} and \mathcal{R}_b represents the set of pixels obtained by excluding \mathcal{R}_o from \mathcal{B} .

Next, we sample pixel features from the sets \mathcal{R}_i , \mathcal{R}_o , \mathcal{R}_f and \mathcal{R}_b . The sampling ratio is set to α . For feature f_i , the sampled features are denoted as k_b^i , k_o^i , k_f^i and k_i^i respectively. Similarly, for feature f_j , the sampled features are denoted as k_b^j , k_o^j , k_f^j and k_i^j respectively.

Then, we calculate the query features of background and foreground across RoIs through:

$$q^b = M(k_b^i, k_o^i, k_b^j, k_o^j), \quad q^f = M(k_f^i, k_i^i, k_f^j, k_i^j),\tag{5}$$

where M represents the averaged operation of vectors.

Finally, to narrow the same category feature distance and expand the feature distance between foreground and background. We calculate four pairs of contrastive losses as follows:

$$L_{cl}^s = CL(q^b, k_b, k_f) + CL(q^b, k_o, k_i) + CL(q^f, k_f, k_b) + CL(q^f, k_i, k_o),\tag{6}$$

where CL represents contrastive learning loss. k_b represents the concatenation of k_b^i and k_b^j . The calculation of CL is described below:

$$CL(q^+, k^+, k^-) = -\log \frac{e^{\cos(q^+, k^+)/\tau}}{e^{\cos(q^+, k^+)/\tau} + \sum_{i=1}^N e^{\cos(q^+, k_i^-)/\tau}},\tag{7}$$

where q^+ and k^+ represent a pair of positive instances, k^- represents a negative instance, and τ is the temperature hyper-parameter.

Different from the previous methods, PC₂Seg (Zhong et al., 2021) extracts positive instance pair of contrastive learning from a single perspective. However, our proposed CRC performs contrastive learning cross-RoI, which enhances the feature generality.

3. Experiments

3.1. Datasets

Our method is evaluated on the Cryosectioned Nuclei Segmentation (CryoNuSeg) dataset (Mahbod et al., 2021), the Digestive-System Pathological Segmentation (DigestPath) dataset (Da et al., 2022), and Multiple Organs Nuclei Segmentation (MoNuSeg) dataset (Kumar et al., 2017). CryoNuSeg contains 30 images from 10 organs, each with a size of 512×512 . DigestPath contains 69 images of the digestive system, each with a size of approximately 1500×1200 . MoNuSeg contains 30 images from 7 organs, each with a size of 1000×1000 .

Table 1: Performance comparisons on CryoNuSeg, DigestPath and MoNuSeg Datasets. The best performance is highlighted in **bold**, and the second-best is underlined. † represents p-value of $AJI < 0.001$ and ‡ represents p-value of $AJI < 0.05$.

Ratio	Methods	CryoNuSeg			DigestPath			MoNuSeg		
		Dice	AJI	PQ	Dice	AJI	PQ	Dice	AJI	PQ
1/8	Mask R-CNN [†] (He et al., 2017)	50.28	26.43	27.17	52.58	29.12	30.87	70.03	48.76	45.29
	MMT-PSM [†] (Zhou et al., 2020a)	54.83	30.17	29.81	55.68	32.34	35.94	73.28	50.14	47.27
	PointWSSIS [†] (Kim et al., 2023)	58.66	35.41	33.61	<u>59.90</u>	40.06	44.10	<u>76.12</u>	<u>50.80</u>	49.34
	ShapeProp [‡] (Zhou et al., 2020b)	57.42	<u>35.53</u>	<u>33.68</u>	58.18	39.94	43.49	75.33	49.89	50.02
	NoisyBoundary [†] (Wang et al., 2022)	55.14	29.57	30.96	58.34	36.75	37.94	75.27	48.14	49.37
	PG-FANet [†] (Jin et al., 2024)	<u>59.06</u>	35.47	32.96	58.20	<u>40.32</u>	<u>44.12</u>	75.17	50.44	<u>51.05</u>
	BASS [†] (Ours)	59.26	36.32	35.09	61.00	41.33	45.07	77.43	51.80	53.05
1/4	Mask R-CNN [†] (He et al., 2017)	62.89	34.17	32.96	53.44	35.12	38.79	72.30	49.30	47.21
	MMT-PSM [†] (Zhou et al., 2020a)	67.24	37.60	34.67	58.23	37.64	41.93	73.14	51.08	49.17
	PointWSSIS [†] (Kim et al., 2023)	75.01	47.12	49.83	64.93	43.16	47.86	<u>75.21</u>	51.11	52.06
	ShapeProp [‡] (Zhou et al., 2020b)	73.37	<u>48.70</u>	48.72	63.31	43.35	48.44	74.86	51.29	52.44
	NoisyBoundary [†] (Wang et al., 2022)	69.34	38.85	35.91	61.15	40.77	45.74	73.13	50.77	51.94
	PG-FANet [†] (Jin et al., 2024)	74.54	47.80	<u>49.93</u>	63.24	<u>43.71</u>	<u>48.76</u>	<u>75.21</u>	<u>52.19</u>	<u>53.33</u>
	BASS [†] (Ours)	<u>74.79</u>	48.96	50.36	<u>63.41</u>	44.72	49.14	76.34	53.39	55.85
1/2	Mask R-CNN [†] (He et al., 2017)	69.31	43.34	42.10	57.17	38.01	42.44	74.92	50.28	50.26
	MMT-PSM [†] (Zhou et al., 2020a)	72.85	45.06	44.47	59.11	39.97	45.58	75.12	51.05	51.17
	PointWSSIS [†] (Kim et al., 2023)	<u>74.67</u>	<u>49.91</u>	49.29	63.87	<u>45.45</u>	51.64	75.89	52.14	52.30
	ShapeProp [‡] (Zhou et al., 2020b)	74.40	48.24	47.55	64.15	45.02	<u>52.93</u>	76.01	51.88	52.94
	NoisyBoundary [†] (Wang et al., 2022)	73.71	46.58	46.13	61.35	44.41	50.65	77.10	53.99	55.20
	PG-FANet [†] (Jin et al., 2024)	72.17	49.86	<u>49.37</u>	<u>64.49</u>	45.14	51.15	78.77	54.91	<u>56.04</u>
	BASS [†] (Ours)	76.76	51.09	49.66	65.72	46.14	53.96	<u>77.80</u>	<u>54.82</u>	56.59

3.2. Implementation Details and Evaluation Metrics

Following the previous method (Graham et al., 2019), we crop all the images to patches of 256×256 pixels with an overlap of 128 pixels for data preprocessing. All experiments are carried out with an RTX 3090 GPU. SGD is used as the optimizer. The learning rate, momentum, and weight decay are set to 0.02, 0.9, and 0.001, respectively. Besides, we evaluate the segmentation performance in terms of Dice (Vu et al., 2019), aggregated Jaccard index (AJI) (Kumar et al., 2017), and panoptic quality (PQ) (Kirillov et al., 2019).

3.3. Comparison with the State of the Art Methods

We compare our proposed BASS against several state-of-the-art methods, including MMT-PSM (Zhou et al., 2020a), PointWSSIS (Kim et al., 2023), ShapeProp (Zhou et al., 2020b), NoisyBoundary (Wang et al., 2022) and PG-FANet (Jin et al., 2024). Besides, to validate the improvement of our semi-supervised model, we also compare our method with supervised

Mask R-CNN. We trained the models using 1/8, 1/4, and 1/2 of the labeled data on ResNet-50. A more detailed data split is presented in the appendix.

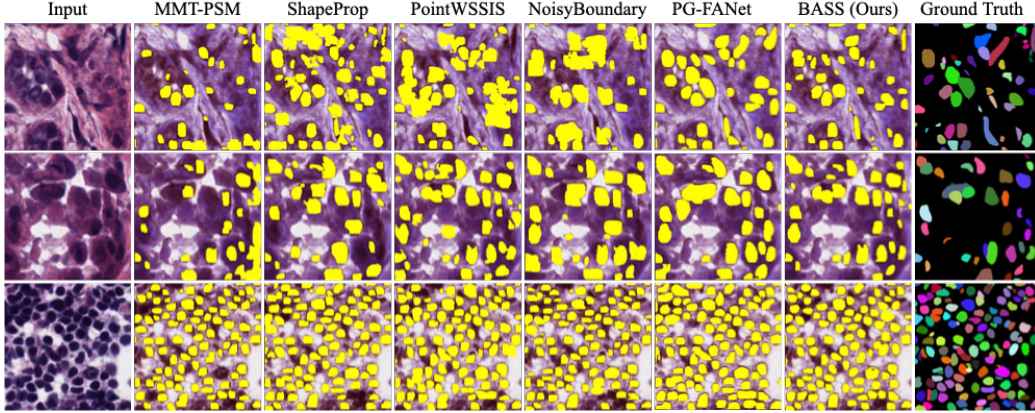


Figure 2: The semi-supervised instance segmentation visualization comparisons.

Quantitative comparison results on three datasets are displayed in Table 1, which shows that our method achieves the optimal performance at all three annotation ratios. Even with only 1/8 of the annotations, our BASS exceeds the suboptimal method approximately 1% in PQ. Fig.2 displays the visual comparison results. We can see that MMT-PSM and NoisyBoundary mistakenly identify nuclei as tissue due to the lack of semantic discrimination between nuclei and tissues. Although ShapeProp and PointWSSIS employ weak labels to enhance the location ability of nuclei, they still have nuclear shape errors.

Table 2: The segmentation head ablation experiments on CryoNuSeg and DigestPath.

NMH	LRD	CRC	CryoNuSeg			DigestPath		
			Dice	AJI	PQ	Dice	AJI	PQ
✓			65.49	40.23	36.94	60.80	44.73	48.54
	✓		64.37	39.24	39.91	61.22	43.09	47.80
✓	✓		<u>72.17</u>	<u>46.44</u>	<u>45.72</u>	<u>63.19</u>	<u>45.86</u>	<u>51.22</u>
✓	✓	✓	76.76	51.09	49.66	65.72	46.14	53.96

3.4. Ablation Studies

Ablation Studies for Segmentation Head. In the student network, we employ three prediction heads, namely, the naive mask head (NMH), low-resolution denoising mask head (LRD), and cross-RoI contrastive learning mask head (CRC), to jointly supervise the segmentation predictions. To evaluate the effectiveness of these heads, we conducted a series of ablation experiments to assess the impact of different designs. Specifically, we compared four designs: NMH, LRD, NMH+LRD, and NMH+LRD+CRC. The experimental results are listed in Table 2. From the table, we can observe the NMH+LRD+CRC outperforms the other methods, indicating that incorporating multiple segmentation constraints is effective.

Ablation Studies for Box and Pixel Thresholds We conduct threshold filtering experiments on the MoNuSeg dataset with a 1/2 annotation ratio, and The experiment results are shown in Tables 3 and 4. Table 3 uses nuclear count statistics to determine the optimal box threshold. We can find that the model performs best when the threshold is set

to 0.38. When changing the value, the model’s performance deteriorated, indicating the effectiveness of using nucleus count for box threshold selection. In addition, Table 4 shows the experiment results of pixel threshold. The table shows that when choosing 0.5 as the threshold, the model achieved optimal performance in terms of Dice and PQ scores.

Table 3: The box threshold setting experiments on MoNuSeg dataset.

Box Thr	Dice	AJI	PQ
0.3	76.37	52.20	54.07
0.38(opt)	77.80	54.82	56.59
0.5	75.68	50.83	53.26
0.7	72.28	48.01	51.58

Table 4: The mask threshold setting experiments on MoNuSeg dataset.

Pixel Thr	Dice	AJI	PQ
0.3	76.12	54.01	55.23
0.4	77.04	54.96	55.37
0.5(opt)	77.80	54.82	56.59
0.6	76.97	54.04	56.21

Ablation Studies for Sampling Ratio α . We conduct sampling ratio experiments and set four sampling ratios of 0.1, 0.3, 0.5, and 0.7 in the CRC. The experimental results are shown in Fig. 3. The table shows that as the sampling ratio increases, the performance gradually improves, indicating that the sampling ratio indeed influences the performance. When the sampling ratio is large, the model obtains more sampled pixels, resulting in better contrastive learning performance. However, as the sampling ratio increases, the computational cost of the model also increases. Therefore, we select 0.7 as the final sampling ratio, which achieves the best balance between model performance and computational cost.

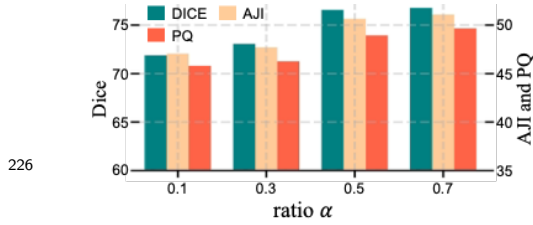


Figure 3: The sampling ratio ablation experiments on CryoNuSeg dataset.

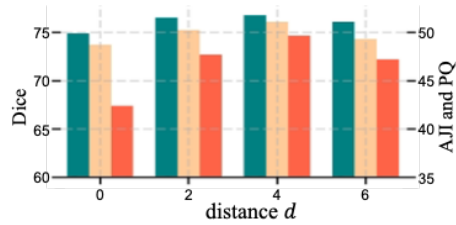


Figure 4: The distance comparison experiments on CryoNuSeg dataset.

Ablation Studies for Distance d . We investigate the effect of distance d , which represents the distance from the inner (outer) contour to the accurate nuclei contour. Expressly, we set d to 0, 2, 4, and 6. It is worth noting when $d = 0$, we do not sample between the actual and inner (outer) contour. From the Fig. 4, we can see when $d = 4$, the model performs best. However, the performance drops as d decreases. This is because when reducing the sampling range, the boundary information obtained by the model also decreases. On the contrary, when d increases to 6, the sampling area becomes more extensive, leading to a mixture of boundary and non-boundary features, ultimately decreasing performance.

4. Conclusions

This paper proposes a boundary-aware contrastive learning model for semi-supervised nuclei segmentation based on the teacher-student framework. In the student network, a low-resolution denoising module and a cross-RoI contrastive learning module are proposed to ease the contour noises of nuclei from coarse and fine aspects. Extensive comparison exper-

iments on two publicity datasets show that the proposed method is superior to the existing semi-supervised instance segmentation methods.

References

- Hao Chen, Xiaojuan Qi, Lequan Yu, and Pheng-Ann Heng. Dcan: deep contour-aware networks for accurate gland segmentation. In *Proceedings of the IEEE conference on Computer Vision and Pattern Recognition*, pages 2487–2496, 2016.
- Qian Da, Xiaodi Huang, Zhongyu Li, Yanfei Zuo, Chenbin Zhang, Jingxin Liu, Wen Chen, Jiahui Li, Dou Xu, Zhiqiang Hu, et al. Digestpath: A benchmark dataset with challenge review for the pathological detection and segmentation of digestive-system. *Medical Image Analysis*, 80:102485, 2022.
- Simon Graham, Quoc Dang Vu, Shan E Ahmed Raza, Ayesha Azam, Yee Wah Tsang, Jin Tae Kwak, and Nasir Rajpoot. Hover-net: Simultaneous segmentation and classification of nuclei in multi-tissue histology images. *Medical image analysis*, 58:101563, 2019.
- Hongliang He, Zhongyi Huang, Yao Ding, Guoli Song, Lin Wang, Qian Ren, Pengxu Wei, Zhiqiang Gao, and Jie Chen. Cdnet: Centripetal direction network for nuclear instance segmentation. In *Proceedings of the IEEE/CVF International Conference on Computer Vision*, pages 4026–4035, 2021.
- Kaiming He, Georgia Gkioxari, Piotr Dollár, and Ross Girshick. Mask r-cnn. In *Proceedings of the IEEE international conference on computer vision*, pages 2961–2969, 2017.
- Reka Hollandi, Nikita Moshkov, Lassi Paavolainen, Ervin Tasnadi, Filippo Piccinini, and Peter Horvath. Nucleus segmentation: towards automated solutions. *Trends in Cell Biology*, 2022.
- Jie Hu, Chen Chen, Liujuan Cao, Shengchuan Zhang, Annan Shu, Guannan Jiang, and Rongrong Ji. Pseudo-label alignment for semi-supervised instance segmentation. In *Proceedings of the IEEE/CVF International Conference on Computer Vision*, pages 16337–16347, 2023.
- Qiangguo Jin, Hui Cui, Changming Sun, Yang Song, Jiangbin Zheng, Leilei Cao, Leyi Wei, and Ran Su. Inter-and intra-uncertainty based feature aggregation model for semi-supervised histopathology image segmentation. *Expert Systems with Applications*, 238:122093, 2024.
- Mahendra Khened, Avinash Kori, Haran Rajkumar, Ganapathy Krishnamurthi, and Balaji Srinivasan. A generalized deep learning framework for whole-slide image segmentation and analysis. *Scientific reports*, 11(1):11579, 2021.
- Beomyoung Kim, Joonhyun Jeong, Dongyoon Han, and Sung Ju Hwang. The devil is in the points: Weakly semi-supervised instance segmentation via point-guided mask representation. In *Proceedings of the IEEE/CVF Conference on Computer Vision and Pattern Recognition*, pages 11360–11370, 2023.

- 278 Alexander Kirillov, Kaiming He, Ross Girshick, Carsten Rother, and Piotr Dollár. Panop-
279 tic segmentation. In *Proceedings of the IEEE/CVF conference on computer vision and*
280 *pattern recognition*, pages 9404–9413, 2019.
- 281 Neeraj Kumar, Ruchika Verma, Sanuj Sharma, Surabhi Bhargava, Abhishek Vahadane,
282 and Amit Sethi. A dataset and a technique for generalized nuclear segmentation for
283 computational pathology. *IEEE transactions on medical imaging*, 36(7):1550–1560, 2017.
- 284 Amirreza Mahbod, Gerald Schaefer, Benjamin Bancher, Christine Löw, Georg Dorffner,
285 Rupert Ecker, and Isabella Ellinger. Cryonuseg: A dataset for nuclei instance segmenta-
286 tion of cryosectioned h&e-stained histological images. *Computers in biology and medicine*,
287 132:104349, 2021.
- 288 Peter Naylor, Marick Laé, Fabien Rey, and Thomas Walter. Segmentation of nuclei in
289 histopathology images by deep regression of the distance map. *IEEE transactions on*
290 *medical imaging*, 38(2):448–459, 2018.
- 291 YCAP Reddy, P Viswanath, and B Eswara Reddy. Semi-supervised learning: A brief
292 review. *Int. J. Eng. Technol*, 7(1.8):81, 2018.
- 293 Carsen Stringer, Tim Wang, Michalis Michaelos, and Marius Pachitariu. Cellpose: a gen-
294 eralist algorithm for cellular segmentation. *Nature methods*, 18(1):100–106, 2021.
- 295 Jesper E Van Engelen and Holger H Hoos. A survey on semi-supervised learning. *Machine*
296 *learning*, 109(2):373–440, 2020.
- 297 Quoc Dang Vu, Simon Graham, Tahsin Kurc, Minh Nguyen Nhat To, Muhammad Shaban,
298 Talha Qaiser, Navid Alemi Koochbanani, Syed Ali Khurram, Jayashree Kalpathy-Cramer,
299 Tianhao Zhao, et al. Methods for segmentation and classification of digital microscopy
300 tissue images. *Frontiers in bioengineering and biotechnology*, page 53, 2019.
- 301 Zhenyu Wang, Yali Li, and Shengjin Wang. Noisy boundaries: Lemon or lemonade for
302 semi-supervised instance segmentation? In *Proceedings of the IEEE/CVF Conference on*
303 *Computer Vision and Pattern Recognition*, pages 16826–16835, 2022.
- 304 Huisi Wu, Zhaoze Wang, Youyi Song, Lin Yang, and Jing Qin. Cross-patch dense contrastive
305 learning for semi-supervised segmentation of cellular nuclei in histopathologic images. In
306 *Proceedings of the IEEE/CVF Conference on Computer Vision and Pattern Recognition*,
307 pages 11666–11675, 2022.
- 308 Yuanyi Zhong, Bodi Yuan, Hong Wu, Zhiqiang Yuan, Jian Peng, and Yu-Xiong Wang.
309 Pixel contrastive-consistent semi-supervised semantic segmentation. In *Proceedings of*
310 *the IEEE/CVF International Conference on Computer Vision*, pages 7273–7282, 2021.
- 311 Yanning Zhou, Hao Chen, Huangjing Lin, and Pheng-Ann Heng. Deep semi-supervised
312 knowledge distillation for overlapping cervical cell instance segmentation. In *Medical Im-*
313 *age Computing and Computer Assisted Intervention–MICCAI 2020: 23rd International*
314 *Conference, Lima, Peru, October 4–8, 2020, Proceedings, Part I 23*, pages 521–531.
315 Springer, 2020a.

- 316 Yanzhao Zhou, Xin Wang, Jianbin Jiao, Trevor Darrell, and Fisher Yu. Learning saliency
317 propagation for semi-supervised instance segmentation. In *Proceedings of the IEEE/CVF*
318 *Conference on Computer Vision and Pattern Recognition*, pages 10307–10316, 2020b.

5. Supplement Materials

5.1. Data Split

In the main body, we used 1/8, 1/4 and 1/2 labeled data to conduct experiments on CryoNuSeg (Mahbod et al., 2021) and DigestPath (Da et al., 2022) datasets respectively.

In this section, we provide the data split details as shown in Table 1. First, these two datasets are divided into the training set, validation set and testing set according to the proportion of 6:2:2. Then, we re-divide the training set into labeled and unlabeled data sets according to 1/8, 1/4 and 1/2. In the whole training process, we keep the validation and testing sets unchanged.

Table 5: The data split on CryoNuSeg and DigestPath datasets.

Dataset	Ratio	Training		Validation	Testing
		Labeled	Unlabeled		
CryoNuSeg	1/8	20	142	54	54
	1/4	40	122	54	54
	1/2	81	81	54	54
DigestPath	1/8	631	2653	835	994
	1/4	930	2354	835	994
	1/2	1740	1554	835	994

5.2. Segmentation head visualization experiments

In this subsection, we provide visual experiments of the naive segmentation head (NMH) and the cross-RoI contrastive learning head (CRC), as shown in Fig.5. By comparing with NMH, it can be observed that the CRC module, utilizing contrastive learning, reduces edge noise and provides clearer boundaries.

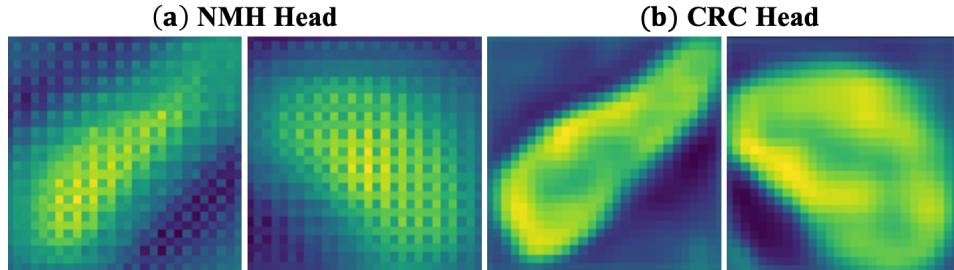


Figure 5: The feature map of prediction. (a) represents naive mask head (NMH); (b) represents cross-RoI contrastive learning head (CRC).

5.3. Comparison experiments

Due to the limited space in the main text, we have provided additional experimental results using ResNet-101 as the backbone in Table 6. From the table, it can be observed that our method outperforms other approaches and achieves the best performance.

Methods	Dice	AJI	PQ	Flops	Para	Iteration	LR	Momen	WD
NoisyBoundary	77.80	54.82	56.59						
Mask R-CNN									
BASS									

Table 6: Performance comparisons on CryoNuSeg and DigestPath Datasets.

Amount of Labels	Method	CryoNuSeg			DigestPath		
		Dice	AJI	PQ	Dice	AJI	PQ
1/8	MMT-PSM (Zhou et al., 2020a)	56.66	33.96	30.81	57.37	36.66	39.55
	PointWSSIS (Kim et al., 2023)	59.24	36.13	35.59	<u>62.91</u>	43.19	46.36
	ShapeProp (Zhou et al., 2020b)	60.07	35.44	35.90	61.22	41.69	<u>46.57</u>
	NoisyBoundary (Wang et al., 2022)	57.12	32.78	34.66	59.11	38.31	40.46
	BASS(Ours)	<u>60.03</u>	36.42	36.06	63.31	<u>42.17</u>	47.25
1/4	MMT-PSM (Zhou et al., 2020a)	71.27	38.98	36.28	60.73	72.22	44.23
	PointWSSIS (Kim et al., 2023)	<u>76.39</u>	48.67	<u>50.96</u>	<u>64.71</u>	43.24	<u>48.48</u>
	ShapeProp (Zhou et al., 2020b)	75.26	<u>48.99</u>	49.79	64.14	<u>44.12</u>	48.00
	NoisyBoundary (Wang et al., 2022)	71.78	40.05	38.31	62.84	43.71	46.56
	BASS(Ours)	76.81	50.72	51.20	65.12	45.87	50.91
1/2	MMT-PSM (Zhou et al., 2020a)	71.58	47.21	48.19	62.79	43.53	50.04
	PointWSSIS (Kim et al., 2023)	<u>76.89</u>	<u>49.31</u>	<u>52.42</u>	<u>65.35</u>	48.26	<u>52.56</u>
	ShapeProp (Zhou et al., 2020b)	76.40	48.11	51.21	64.26	46.04	51.64
	NoisyBoundary (Wang et al., 2022)	74.02	48.13	49.34	64.41	47.23	52.18
	BASS(Ours)	77.14	51.06	54.39	66.89	<u>48.10</u>	55.59